doi: 10.4149/gpb_2024043

Silencing Map3k7 suppresses pyroptosis to alleviate bronchopulmonary dysplasia through inhibiting the TGF-β1/Smad3 pathway

Hong Zhen[1], Qiaozhen Wei[1], Bingmei Wei[1], Qingmei Huang[1] and Ruishan Li[1]

[1] *Department of Pediatrics, The Second Affiliated Hospital of Guangxi Medical University, Nanning, Guangxi Province, China*

Abstract. Bronchopulmonary dysplasia (BPD) is a serious complication in premature infants. This study aimed to investigate the mechanism of mitogen-activated protein 3 kinase 7 (Map3k7) affecting BPD by regulating caspase-1 mediated pyroptosis. The morphology of the lung tissue was observed using hematoxylin–eosin staining. TUNEL staining was performed to detect tissue apoptosis. RNA-seq and protein–protein interaction (PPI) network were performed to identify hub genes. Cell viability and apoptosis was analyzed using the CCK-8 assay and flow cytometry, respectively. Pyroptosis-related factors, inflammatory factors, oxidative stress indicators, and pathway-related proteins were detected using ELISA, qRT-PCR, and Western blotting. Hyperoxia-induced neonatal rats showed alveolar simplification with increased alveolar lumen, and decreased density of secondary alveolar cristae, demonstrating the successful BPD model. Map3k7 was identified as the crucial gene that was upregulated in BPD. Silencing Map3k7 promoted cell proliferation and suppressed apoptosis, inflammation, oxidative stress, and pyroptosis in hyperoxia-induced AEC-II, and alleviated BPD progression in hyperoxia-induced rats. Furthermore, silencing Map3k7 inhibited the TGF-β1/Smad3 pathway, and SRI-011381, the TGF-β pathway activator, weakened the inhibitory effects of silencing Map3k7 on hyperoxia-induced AEC-II. Silencing Map3k7 suppressed pyroptosis to alleviate BPD through inhibiting the TGF-β1/Smad3 pathway, providing a direction for the treatment of BPD in premature infants.

Key words: Bronchopulmonary dysplasia — Pyroptosis — RNA-seq — Map3k7 — TGF-β1/Smad3 pathway

Introduction

Bronchopulmonary dysplasia (BPD), also known as neonatal chronic lung disease, is common in newborns with low gestational age. The morbidity of BPD increases with low gestational age and birth weight (Jensen et al. 2014). Infants born at <25 weeks of age have the highest risk of BPD (Shukla et al. 2021). Preterm birth can result in poor alveolar formation, reduced lung surface area for gas exchange, and BPD (Baker et al. 2014). BPD not only damages the lungs of premature infants, but also manifests as significant pulmonary sequelae with growth (Bhandari et al. 2006). Therefore, prevention of BPD is important.

Mitogen-activated protein 3 kinase 7 (Map3k7), a serine/threonine protein kinase, is a vital part of the MAPK signaling pathway. Activated Map3k7 can phosphorylate multiple target proteins, triggering different signal transduction pathways and participating in the regulation of cell survival, inflammation, and cancer occurrence (Mihaly et al. 2014; Mukhopadhyay et al. 2020; Xu et al. 2020).

Electronic supplementary material. The online version of this article (doi: 10.4149/gpb_2024043) contains Supplementary material.

Correspondence to: Hong Zhen, No. 166, Daxue East Road, Xixiangtang District, Nanning, Guangxi Province, 530007, China
E-mail: zhenhongzh@163.com

miR-203 inhibits NF-κB signaling by targeting Map3k7 and PI3KCA, contributing to the initiation of chronic obstructive pulmonary disease (COPD) (Shi et al. 2015). Map3k7 is essential in cigarette smoke extract-induced ERK-1/2 and NF-κB signaling, and can be identified as a new target for inhibiting inflammatory responses involved in cigarette smoke-induced COPD progression (Pera et al. 2012). Focal adhesion kinase can also interact with Map3k7 and activate the Map3k7–NF-κB pathway to mediate lipopolysaccharide (LPS)-induced inflammatory lung injury (Chen et al. 2022). Currently, the mechanism by which Map3k7 regulates BPD in premature infants remains unclear.

Pyroptosis is a natural immune response of the human body. Several proteins are essential for pyroptosis, including caspase-1/4/5/11, Gasdermin D (GSDMD) and inflammasomes (Shi et al. 2017). Pyroptosis induced by caspase-1 is triggered by a series of inflammasome recognition receptors. The inflammasome consists of pro-caspase-1, apoptosis-associated speck-like proteins (ASC), and pattern recognition receptors (Lamkanfi et al. 2014; Guo et al. 2015). Studies have confirmed that various lung diseases are related to pyroptosis, including COPD, acute lung injury (ALI), asthma, pulmonary fibrosis, and bronchial dysplasia (Eltom et al. 2014; Hussain et al. 2014; Wu et al. 2015; Cheng et al. 2018; Li et al. 2018). Inhibition of alveolar macrophage pyroptosis alleviates LPS-induced ALI in mice (Wu et al. 2015). Liu and his colleagues conclude that pyroptosis might participate in the occurrence and development of COPD (Liu et al. 2023). Inhibition of GSDMD-dependent pyroptosis attenuates silica-induced lung inflammation and fibrosis progression (Song et al. 2022). Transforming growth factor beta (TGF-β1) is a crucial cytokine in BPD pathogenesis (Kwong et al. 2006) and may be involved in the regulation of pyroptosis (Xie et al. 2022; Wang et al. 2023). However, whether Map3k7 affects BPD in premature infants by regulating pyroptosis and the TGF-β1/Smad3 pathway is unclear.

In this study, the effect of Map3k7 on BPD was investigated by transcriptome sequencing and construction of animal and cell models, and the mechanism of Map3k7 in pyroptosis was explored. We systematically elucidated the mechanism of Map3k7 regulating BPD through caspase-1 mediated pyroptosis and TGF-β1/Smad3 pathway, and provided a research direction for the precaution and therapy of BPD.

Materials and Methods

Lentiviral transfection

The shRNA silencing Map3k7 (sh-Map3k7) was designed and subcloned into the GV248 (hU6-MCS-Ubiquitin-IRES-puromycin) vector and mixed with the lentiviral packaging plasmid. An empty vector was used as the negative control (sh-NC).

Construction of BPD models

Pregnant Sprague-Dawley rats (SPF Biotechnology, Beijing, China) were raised under specific pathogen-free standard conditions with free access to food and drink. Newborn rats were randomly divided into the normal (control) and BPD model groups: BPD, BPD+LV-shNC and BPD+LV-shMap3k7 ($n = 6$). Pups in the control group were fed in a conventional atmosphere for 21 days. BPD pups were fed in an organic glass cabin with 85% O_2 for 21 days (Zhang et al. 2023). To prevent oxygen poisoning, the rats in the four groups were rotated daily. On days 10, 14, and 21 after natural delivery, the lung tissues and serum were collected from the pups for analysis. All the pups were perfused with saline and then with 4% paraformaldehyde to fix the tissues. The thoracic cavities of pups were incised to extract both lungs, which were promptly frozen in liquid nitrogen for subsequent experiments.

To explore the effects of Map3k7 on pups with BPD, neonatal pups were raised to 1 week of age and injected with lentiviral particles expressing the negative control and Map3k7. Lentivirus (LV) was injected through the tail vein with a volume of 30 μl at 1×10^8 TU at a time interval of 3 days. These experiments were conducted in the BSL-2 laboratory. On day 21 after natural delivery, all the pups were anesthetized using isoflurane inhalation and sacrificed.

Animal ethics

The study protocol was approved by the Ethics Review Committee of the Second Affiliated Hospital of Guangxi Medical University (2022, KY-0095). All procedures were performed in accordance with the Declaration of Helsinki and relevant national policies.

Hematoxylin-eosin (HE) staining

Tissues were fixed in 4% paraformaldehyde, embedded in paraffin, and then cut into 4-μm tissue sections using a paraffin microtome. Dried slices were immersed in xylene I, xylene II, anhydrous ethanol I, anhydrous ethanol II, and alcohol (95%, 80%, and 70%). Subsequently, the sections were stained with hematoxylin, washed, and soaked in 1% hydrochloric acid ethanol. Slices were treated with 50%, 70%, and 80% alcohol. The slices were then immersed in eosin solution; treated with 95% ethanol, ethanol I, ethanol II, xylene I, and xylene II; sealed with neutral gum; and observed under a biological inverted microscope. The radial alveolar count (RAC) and mean linear intercept (MLI) were measured using

the ImageJ software (National Institutes of Health, Bethesda, MD, USA). Five lines were drawn in each field of view, and MLI was calculated. MLI is length of each line/number of alveolar intercepts of the line.

TUNEL staining

Lung tissue apoptosis was detected using a TUNEL Apoptosis Detection Kit (Beyotime, Shanghai, China). The paraffin sections were deparaffinized with xylene and rinsed with phosphate-buffered saline (PBS). The sections were then incubated with proteinase K (20 μg/ml) without DNase at 37°C for 30 min to improve the accessibility of the TUNEL reagents. The sections were then washed and incubated with H_2O_2 to block endogenous peroxidase activity. Next, TUNEL reagent was applied, and the sections were incubated in the dark at 37°C for 60 min to label the fragmented DNA. Subsequently, the sections were stained with 4',6-diamidino-2-phenylindole to visualize labeling. After counterstaining with hematoxylin, the sections were sealed and examined under a fluorescence microscope (Olympus, Tokyo, Japan) to observe apoptotic cells.

Enzyme linked immunosorbent assay (ELISA)

Corresponding ELISA kits (Esebio, Shanghai, China) were bought to test the levels of lactic dehydrogenase (LDH) release, caspase-1 activity, IL-6, TNF-α, IL-1β, IL-18, MDA, SOD, and ROS in the collected serum or cell culture supernatant according to the instructions. The absorbance (OD value) at 450 nm wavelength was measured using an ELISA reader.

Western blot

Proteins of samples were isolated by radioimmunoprecipitation assay buffer. After sodium dodecyl-sulfate polyacrylamide gel electrophoresis, the protein was transferred to the polyvinylidene fluoride (PVDF) membrane at 4°C for 2 h. Samples were then blocked with 5% skim milk–Tris-buffered saline (TBST) at room temperature for 2 h with shaking. After blocking, the PVDF membrane was washed with washing solution, and added with primary antibodies, including anti-NLRP3 (ab263899, 1/1000, Abcam, Cambridge, MA, USA), anti-caspase-1 (ab207802, 1/1000, Abcam), anti-ASC (ab283684, 1/1000, Abcam), anti-GSDMD (ab210070, 1/1000, Abcam), anti-Map3k7 (ab50431, 1/1000, Abcam), anti-TGF-β1 (ab315254, 1/1000, Abcam), anti-Smad3(ab40854, 1/1000, Abcam), anti-p-Smad3 (ab63403, 1/1000, Abcam), and anti-β-actin (ab5694, 1/1000, Abcam). Then, the membrane was incubated all night with shaking at 4°C. Subsequently, the PVDF membrane was washed three times with TBST for 10 min each time and incubated with goat anti-rabbit antibody for 1 h with shaking at room temperature. Eventually, the membrane was added to the membrane, and images were obtained using a Tanon 5200 Chemiluminescent Imaging System (Shanghai, China). The gray values of the bands were evaluated using the ImageJ software.

RNA-seq

RNA was extracted from lung tissue samples of the control and BPD groups using a TRIzol reagent (Invitrogen, USA) (Sigma-Aldrich, St. Louis, MO, USA). Library construction was performed using the VAHTS Universal V10 RNA-seq Library Prep Kit (Vazyme, Nanjing, China) following the manufacturer's recommendations, and sequenced on the Illumina HiSeq platform. Raw data were processed using Perl scripts to filter out low-quality reads. Differentially expressed genes (DEGs) were screened using $|\log_2\text{FoldChange}| > 1$ and p-value < 0.05. Volcano plots of DEGs were drawn using the ggplots2 package in R. Bicluster analysis was performed using the R heatmap package.

The DEGs were categorized into molecular function (MF), biological process (BP), and cellular component (CC) categories for Gene Ontology (GO) analysis. The top six enriched GO terms with the smallest p-values in each GO category were selected for display. Kyoto Encyclopedia of Genes and Genomes (KEGG) enrichment analysis was performed on the DEGs, and the degree of enrichment was measured based on the enrichment factor, false discovery rate (FDR) value, and number of genes enriched in the pathway. The top 20 enriched KEGG pathways with the smallest FDR values were selected for further analysis.

STRING (https://www.string-db.org/) was used to analyze DEGs and predict the interactions between proteins that may play a key role in disease pathogenesis. The interaction score was set to 0.400 as the significance standard.

Quantitative real-time PCR (qRT-PCR)

Total RNA from each group was extracted using a TRIzol reagent (Invitrogen) following the manufacturer's instructions. Then, RNA was reverse transcribed into cDNA by PrimeScript™ RT Master Mix (Takara, Beijing, China) using a PCR Amplifier, and qRT-PCR was executed by AceQ qPCR SYBR Green Master Mix (Vazyme, Nanjing, China) using an ABI7500 Real-time PCR (Applied Biosystems, USA). The reaction conditions were pre-denaturation at 95°C for 30 s, followed by denaturation at 95°C for 10 s, and annealing at 60°C for 30 s for 40 cycles. The Ct value obtained was analyzed using the $2^{-\Delta\Delta Ct}$ method. Primers were synthesized by Sangon (Shanghai, China), and the sequences used are listed in Supplementary material (Table S1). Glyceraldehyde-3-phosphate dehydrogenase was used as the internal control.

Cell culture and treatment

Type II alveolar epithelial cells from rats (AEC-II) obtained from iCell (Shanghai, China) were divided into the control, hyperoxia, hyperoxia+LV-sh-NC, and hyperoxia+LV-sh-Map3k7 groups. For the control group, cells were incubated in Dulbecco's modified eagle medium (DMEM) (21% O_2/5% CO_2) for 24 h, and cells in the other groups were exposed to hyperoxia (85% O_2/5% CO_2) and incubated in DMEM for 48 h at 37°C.

Hyperoxia-induced AEC-II cells were treated with sh-NC and sh-Map3k7 using Lipofectamine 3000 for 48 h. Stable cells were selected by adding puromycin (5.0 μg/ml). In addition, the AEC-II cells were treated with the TGF-β pathway activator, SRI-011381 (10 μM) for 48 h.

CCK-8 assay

Cell proliferation in each group was detected using the CCK-8 Kit (Solarbio, Beijing, China) at 1, 2, 3, and 4 days after transfection. Cells in each group were seeded in 96-well plates with 100-μl cell suspension (1.5×10^4/well) and incubated at 37°C until 80% confluency was reached. The maintenance medium (2% fetal bovine serum + 98% DMEM) was replaced. After incubating the plate for 24 h, the culture medium was removed, and the cells were washed twice with Dulbecco's phosphate-buffered saline. Then, each well was added with 90 μl of maintenance medium and 10 μl of CCK-8 solution. After incubation for 2 h, absorbance was measured at 450 nm using an ELISA reader.

Apoptosis rate

The cells were centrifuged at 1000×*g* for 5 min, the supernatant was discarded, and Annexin V-FITC was added. The cells were then incubated with propidium iodide solution at room temperature for 15 min in the dark. Apoptosis was detected by flow cytometry (Cytoflex, BD Biosciences, USA).

ROS measurement

Intracellular ROS production was detected by 2,7-dichlorofluorescein diacetate (DCFH-DA, Beyotime, Shanghai, China). Cells were seeded and grown in a 12-well plate. Cells were washed twice with PBS and incubated with 10 μM DCFH-DA solution for 15 min. Images were captured using a fluorescence microscope (Nikon).

Statistical analysis

All data were processed using GraphPad Prism 8.0 and presented as means ± standard deviations. A *t*-test was used for comparisons between two groups, whereas a one-way analysis of variance was performed for multiple groups. Tukey's multiple comparison test was used for pairwise comparisons. Significance was set at $p < 0.05$.

Results

Successful construction of BPD models

The lung tissue morphology of rats in the control and BPD groups was observed on days 10, 14, and 21 after birth by HE staining (Fig. 1A). Compared with the lung structure of the control group, that of the BPD group had typical features of simplified alveoli, which were most evident on day 21, with an increased alveolar cavity and decreased alveoli. Moreover, rats in the BPD group showed a decrease in the density of the alveolar secondary ridge and gradual thickening of the alveolar wall (Fig. 1A), with elevated MLI and reduced RAC (Fig. 1B,C).

To further investigate the successful construction of the BPD model, ELISA was performed to detect the expression of inflammatory factors and oxidative stress-related indicators in the serum of both groups of rats. On days 10, 14, and 21 after birth, MDA and ROS levels were significantly increased in the model group, whereas SOD levels were lower than those in the control group (Fig. 1D). In addition, the TNF-α, IL-6, IL-18, and IL-1β levels in the BPD group were significantly increased (Fig. 1E). Thus, inflammation and oxidative stress in the BPD group were significantly higher than those in the control group on days 10, 14, and 21 after birth, with the most significant increase on day 21. Moreover, cell apoptosis on day 21 after birth was evaluated by TUNEL staining, which showed that cell apoptosis was significantly increased in the BPD group compared with that in the control group (Fig. 1F).

RNA-seq and screening of DEGs

On day 21 after birth, lung tissue samples from the control (C21dL) and model groups (M21dL) were collected, with three samples in each group, and RNA-seq was performed. A total of 233 genes were significantly differentially expressed between the two groups, with 109 genes showing significant upregulation, and 124 genes showing significant downregulation. The top ten upregulated and downregulated DEGs are listed in Table S2. A volcano plot and cluster diagrams of the DEGs are presented in Figure 2A and B.

GO enrichment analysis was performed on the DEGs. The top six GO terms in each GO classification were selected for display analysis. GO analysis revealed that DEGs were mainly enriched in the extracellular space and extracellular region in

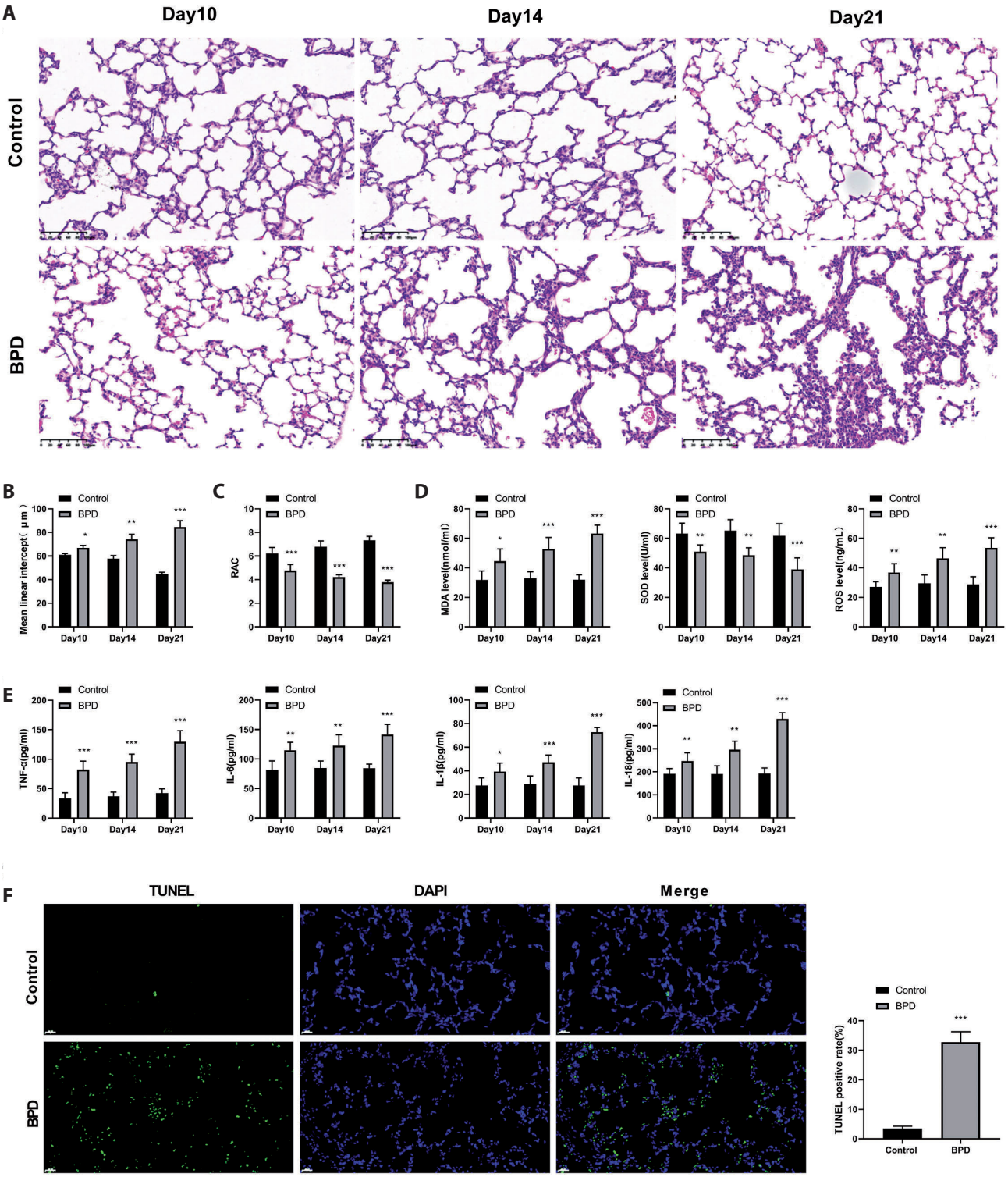

Figure 1. The lung tissue structure, inflammatory factors, and oxidative stress indicators of rats in Control group and bronchopulmonary dysplasia (BPD) group were detected. **A.** Images of lung tissue of rats on the 10th, 14th and 21st day after birth with Hematoxylin-eosin staining (scale: 100 μm, magnification: 200×). **B.** Mean linear intercept (MLI). **C.** Radial alveolar count (RAC). **D.** Oxidative stress-related indicators (MDA, SOD and ROS) were detected by ELISA. **E.** The expressions of inflammatory factors (TNF-α, IL-6, IL-18 and IL-1β) were detected by ELISA. **F.** TUNEL fluorescence staining was used to detect apoptosis in the lung tissue of rats on the 21st day after birth in each group (scale: 20 μm, magnification: 400×). * $p < 0.05$, ** $p < 0.01$, *** $p < 0.001$ *vs.* Control ($n = 6$).

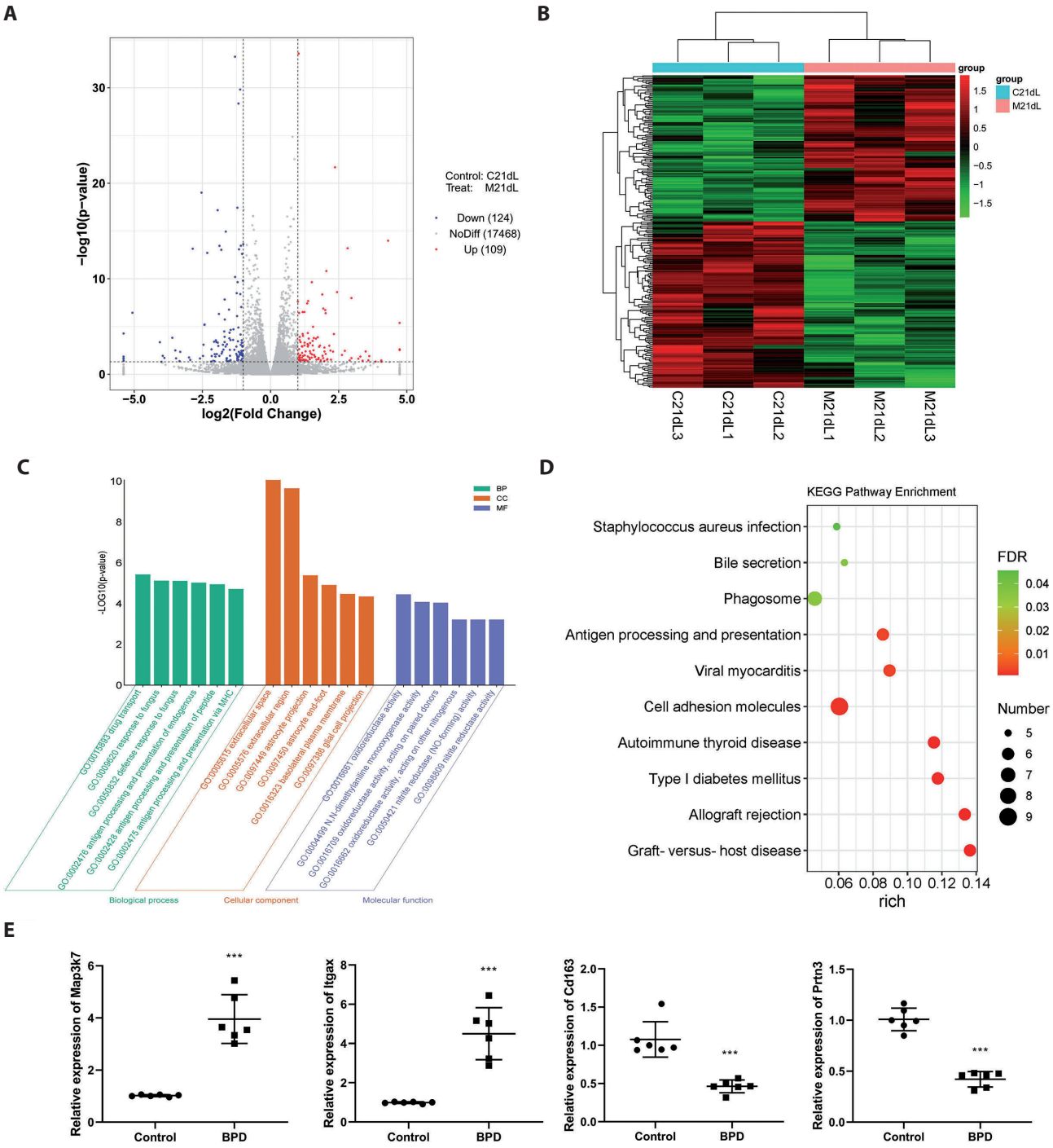

Figure 2. Analysis of differentially expressed genes (DEGs). **A.** Volcano plot of DEGs, the coordinate is $\log_2$FoldChange, and the ordinate is −log10 (*p*-value). Red dots represent up-regulated genes in this group, blue dots represent down-regulated genes in this group, and gray dots represent non-significant DEGs. **B.** Cluster diagram of DEGs. Note: Horizontal represents genes, each column is a sample, red represents high expression genes, and green represents low expression genes. **C.** Histogram of GO enrichment analysis of DEGs. BP, biological process; CC, cellular components; MF, molecular function. The ordinate is −log10 (*p*-value). **D.** Bubble plot of KEGG enrichment analysis of DEGs. The color depth of the node indicates the FDR value, and the size of the node refers to the number of genes. **E.** qRT-PCR validation of DEGs (Map3k7, Prtn3, Itgax, Cd163). *** $p < 0.001$ *vs.* Control ($n = 6$). (See online version for color figure.)

CC, oxidoreductase activity, N,N-dimethylaniline monooxygenase activity in MF, and drug transport and response to fungus in BP (Fig. 2C). KEGG enrichment analysis of the DEGs is shown in Figure 2D. DEGs were mainly enriched in graft-*versus*-host disease, allograft rejection, type I diabetes mellitus, autoimmune thyroid disease, and cell adhesion molecules. Top 20 GO terms and top 10 KEGG terms are shown in Table S3 and S4.

Subsequently, a PPI network was constructed using the STRING database based on the DEGs (Fig. S1). Among these highly interconnected DEGs, Map3k7, Prtn3, Itgax, and Cd163 were associated with pyroptosis and were selected as candidate genes for further analysis.

qRT-PCR was performed to validate the expression of candidate genes in the different groups (Fig. 2E), demonstrating that, in alignment with the sequencing data, Map3k7 and Itgax expressions were significantly upregulated, whereas Prtn3 and Cd163 expressions were significantly downregulated in BPD rats. Based on literature, Map3k7 was selected as the target gene for further studies.

Silencing Map3k7 promoted cell proliferation and inhibited apoptosis, inflammation, and oxidative stress in vitro

The efficiency of Map3k7 silencing was detected by Western blotting, which showed that compared with the hyperoxia group, the hyperoxia+LV-shMap3k7 group demonstrated significantly reduced Map3k7 expression, indicating the effectiveness of Map3k7 silencing (Fig. 3A). CCK-8 assay and flow cytometry were conducted to detect cell proliferation and apoptosis, respectively. Compared with the control, hyperoxia significantly inhibited cell proliferation and contributed to cell apoptosis, and knockdown of Map3k7 significantly increased cell proliferation and suppressed apoptosis caused by hyperoxia treatment (Fig. 3B,C).

To elucidate the effects of Map3k7 on pulmonary inflammatory response and oxidative stress, we performed ELISA analysis, illustrating that the concentrations of IL-6, TNF-α, IL-18, and IL-1β in the hyperoxia group were significantly elevated compared with those in the control group. The IL-1β, IL-6, IL-18, and TNF-α expression levels in the hyperoxia+LV-shMap3k7 group were significantly lower than those in the hyperoxia+LV-shNC group ($p < 0.001$, Fig. 3D). These results indicate that silencing Map3k7 inhibited the increase in inflammatory factors induced by hyperoxia. Meanwhile, an increase in MDA and ROS levels as well as a decrease in SOD after hyperoxia was observed, although silencing Map3k7 reduced MDA and ROS levels and increased SOD (Fig. 3E). Similarly, intracellular ROS levels were detected by fluorescence staining, further showing that silencing Map3k7 inhibited the oxidative stress caused by hyperoxia (Fig. 3F).

Silencing Map3k7 inhibited pyroptosis induced by hyperoxia

ELISA kits were used to measure LDH release and caspase-1 activity. Compared with the control, hyperoxia contributed to the release of LDH and caspase-1 activity, whereas silencing Map3k7 significantly weakened it (Fig. 4A,B). Furthermore, the expressions of GSDMD, ASC, NLRP3, and caspase-1 were significantly increased in the hyperoxia group than those in the control group. Compared with hyperoxia+LV-shNC, silencing Map3k7 significantly reduced the expression of GSDMD, NLRP3, and caspase-1 (Fig. 4C,D). In conclusion, hyperoxia induced pyroptosis, whereas silencing Map3k7 reversed this phenomenon.

Silencing Map3k7 inhibits TGF-β/Smad3 pathway to alleviate BPD in vitro

TGF-β/Smad3 pathway related proteins were detected by Western blots, showing that compared with the control group, the hyperoxia group had increased TGF-β1 and P-Smad3 levels, and silencing Map3k7 significantly inhibited the TGF-β/Smad3 pathway (Fig. 5A). To further explore the function of the TGF-β/Smad3 pathway in hyperoxia-induced AEC-II, the TGF-β pathway activator, SRI-011381, was applied for feedback experiments. The CCK-8 assay demonstrated that SRI-011381 inhibited the effect of silencing Map3k7 on the activity of hyperoxia-induced AEC-II cells (Fig. 5B). Similarly, SRI-011381 reversed the inhibitory effects of silencing Map3k7 on apoptosis, inflammatory factors (IL-1β, IL-6, IL-18, and TNF-α), and oxidative stress (MDA, SOD, and ROS) in hyperoxia-induced AEC-II cells (Fig. 5C–H).

Silencing Map3k7 suppresses pyroptosis by inhibiting the TGF-β/Smad3 pathway in vitro

LDH release, caspase-1 activity, and pyroptosis-related proteins were detected by the corresponding ELISA kits and Western blotting, which demonstrated that silencing Map3k7 suppressed pyroptosis in hyperoxia-induced AEC-II cells. Meanwhile, SRI-011381 reversed the inhibitory effects of silencing Map3k7 on pyroptosis (Fig. 6A–C).

Silencing Map3k7 alleviates BPD progression in vivo

To further investigate the effects of Map3k7 on BPD progression, we transfected Map3k7 shRNA into BPD neonatal rats on postnatal day 7 to knockdown Map3k7 expression. Western blotting was employed to assess Map3k7 expression levels, which showed that compared with the BPD group, the BPD+LV-shNC group did not demonstrate a signifi-

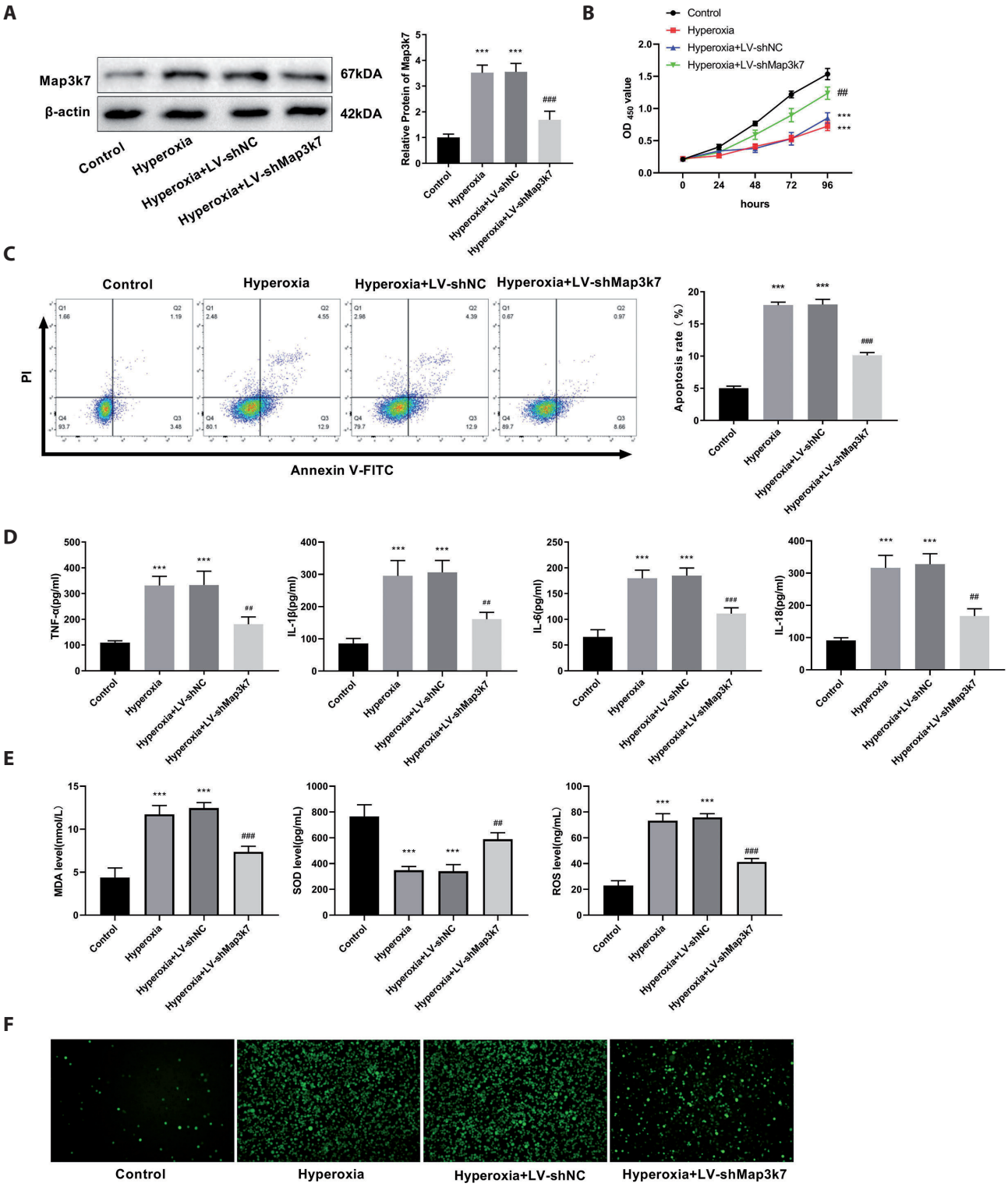

Figure 3. The regulation of Map3k7 was verified *in vitro*. **A.** Western blot was used to detect Map3k7 silencing efficiency. **B.** CCK-8 was performed to detect cell proliferation. **C.** Cell apoptosis was measured by flow cytometry. **D.** ELISA was performed to detect the level of inflammatory factors (TNF-α, IL-6, IL-18 and IL-1β). **E.** ELISA was performed to detect the level of oxidative stress-related indicators (MDA, SOD and ROS). **F.** DCFH-DA fluorescence staining was performed to detect intracellular reactive oxygen species (ROS). *** $p < 0.001$ *vs.* control; ### $p < 0.001$ ## $p < 0.01$ *vs.* Hyperoxia+LV-shNC ($n = 3$).

cant difference in Map3k7 expression. By contrast, Map3k7 expression was significantly reduced in the BPD+LV-sh Map3k7 group, indicating efficient knockdown, compared with that in the BPD+LV-shNC group (Fig. 7A). Furthermore, silencing Map3k7 improved pulmonary injury in BPD rats, as evidenced by a decreased MLI and increased RAC (Fig. 7B,C), along with a reduction in cell apoptosis in the lung tissue (Fig. 7D). Additionally, the downregulation of Map3k7 decreased the expression levels of inflammatory factors (TNF-α, IL-6, IL-18 and IL-1β), MDA, and ROS and elevated SOD levels in BPD rats (Fig. 7E,F). Thus, Map3k7 knockdown alleviated BPD progression *in vivo*.

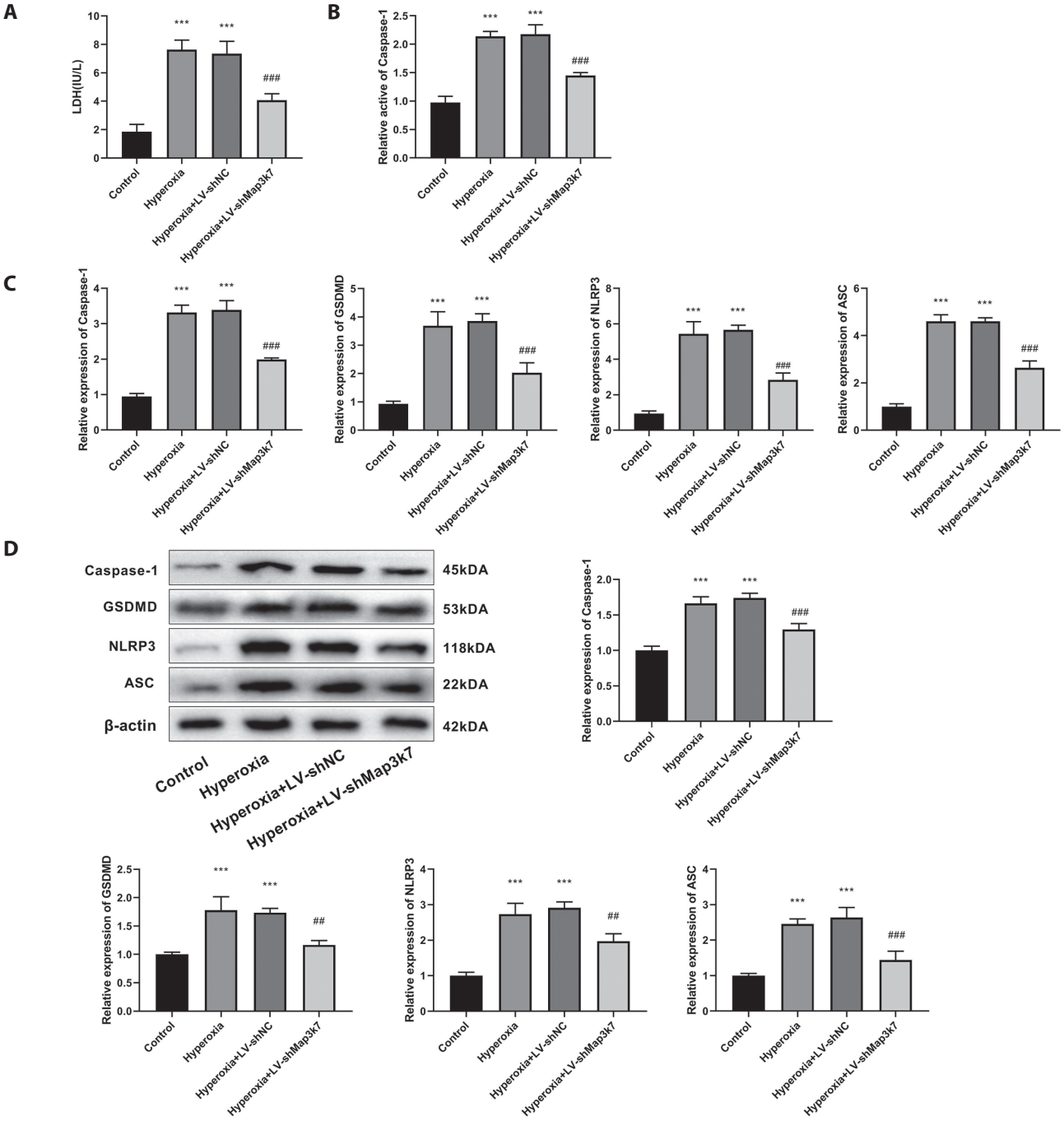

Figure 4. Silencing Map3k7 inhibited pyroptosis. **A.** ELISA was performed to measure LDH release. **B.** Caspase-1 activity was detected. **C.** qRT-PCR was used to detect the expression of factors related to pyroptosis. **D.** Western blot was executed to detect the expression of pyroptosis related proteins. *** $p < 0.001$ *vs.* control; ### $p < 0.001$, ## $p < 0.01$ *vs.* Hyperoxia+LV-shNC ($n = 3$).

Discussion

BPD generally occurs in premature infants, primarily owing to lung immaturity (Shukla et al. 2021). To date, no effective or safe therapy has been established for BPD. Many studies have confirmed the close association of pyroptosis with various lung and respiratory diseases (Eltom et al. 2014; Hussain et al. 2014; Wu et al. 2015; Cheng et al. 2018; Li et al. 2018). In this study, DEGs were screened by transcriptome sequencing, and Map3k7 was obtained by PPI analysis. Silencing Map3k7 promoted cell proliferation, inhibited inflammation, oxidative stress, and pyroptosis in hyperoxia-induced BPD, and SRI-011381, the TGF-β pathway activator, weakened the situation.

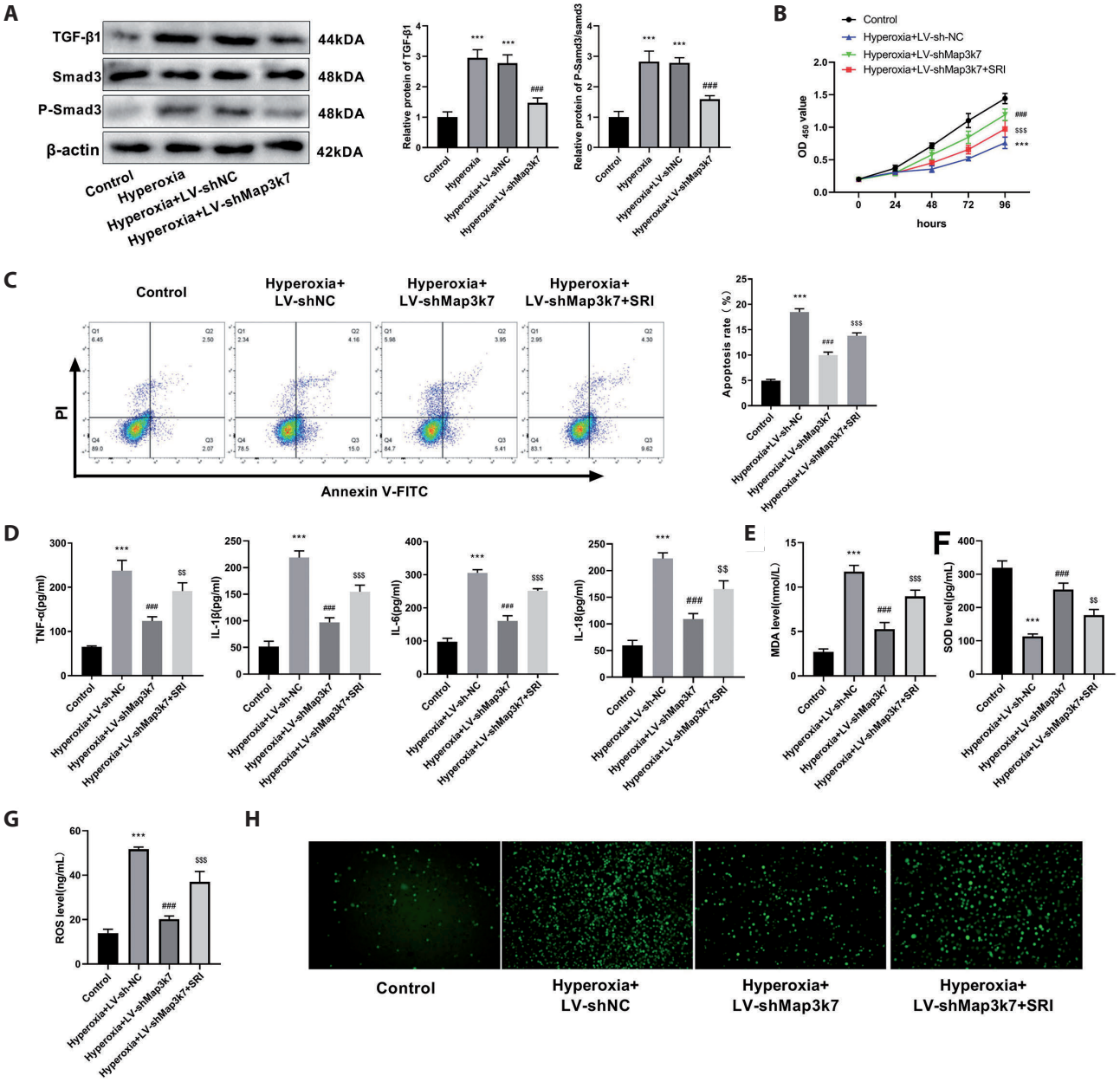

Figure 5. Silencing Map3k7 inhibited TGF-β/Smad3 pathway to alleviate BPD *in vitro*. **A.** Western blot was used to detect expression of TGF-β/Smad3 pathway related proteins. **B.** CCK-8 assay was performed to detect cell viability. **C.** Cell apoptosis was measured by flow cytometry. **D.** ELISA was carried out to detect levels of inflammatory factors (TNF-α, IL-6, IL-18 and IL-1β). **E-G.** ELISA detection of oxidative stress indicator (MDA, SOD and ROS) levels. **H.** DCFH-DA fluorescence staining was performed to detect reactive oxygen species (ROS) level. *** $p < 0.001$ *vs.* Control; ### $p < 0.001$ *vs.* Hyperoxia+LV-shNC; $$ $p < 0.01$, $$$ $p < 0.001$ *vs.* Hyperoxia+LV-shMap3k7 ($n = 3$).

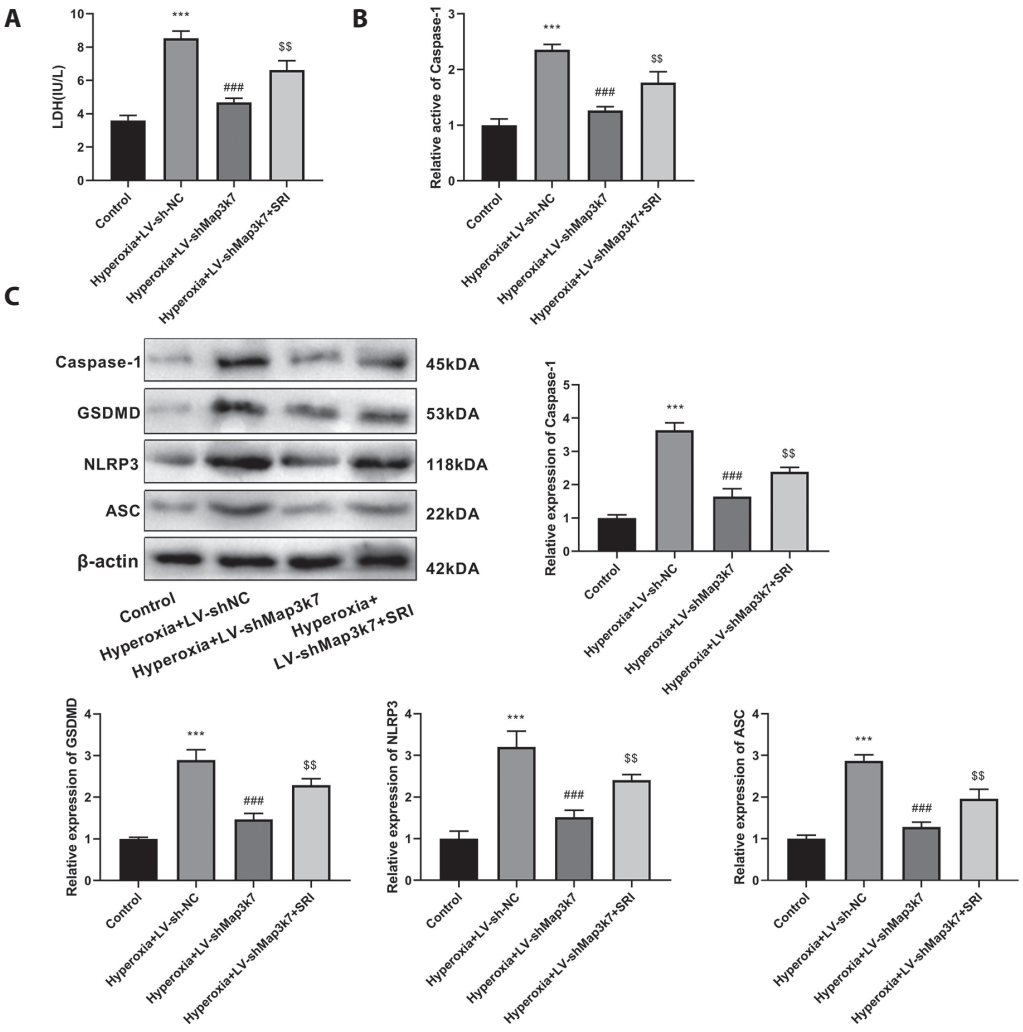

Figure 6. Silencing Map3k7 suppressed pyroptosis by inhibiting the TGF-β/Smad3 pathway *in vitro*. **A.** ELISA kit was carried to measure LDH release. **B.** Caspase-1 activity was detected by corresponding kit. **C.** Western blot was executed to detect the expression of pyroptosis related proteins. *** $p < 0.001$ *vs.* Control; ### $p < 0.001$ *vs.* Hyperoxia+LV-shNC; $$ $p < 0.01$, $$$ $p < 0.001$ *vs.* Hyperoxia+LV-shMap3k7 ($n = 3$).

Transcriptome analysis is increasingly used to identify potential biomarkers and elucidate the pathogenesis and mechanisms related to pulmonary diseases (Hurskainen et al. 2021). In this study, Map3k7, Prtn3, Itgax, and Cd163 were identified using the PPI network. They were associated with pyroptosis and closely related to BPD progression. The proteinase 3 encoded by Prtn3, is a serine protease secreted by neutrophils (Crisford et al. 2018). Studies have indicated that in BPD, the transformation of proteinase-3 leads to a significant increase in IL-8 activity, which is associated with the development of BPD in premature infants (Chakraborty et al. 2014). Itgax, fully named as integrin subunit alpha X, also known as CD11c, is activated in resident alveolar macrophages differentiating into cell populations expressing CD45, CD11c, and SiglecF in a hyperoxic BPD mouse model, resulting in structural developmental disorders in immature lungs (Kalymbetova et al. 2018). CD163, an anti-inflammatory macrophage marker, is downregulated during hyperoxic lung injury (Kwon et al. 2019). Map3k7 is an intracellular hub molecule that regulates p38, NF-κB, and TGF-β signaling pathway (Yamaguchi et al. 1995; Takaesu et al. 2003; Ajibade et al. 2013). Currently, Map3k7 has been confirmed to be involved in various lung diseases. Eupalinolide B inhibits NF-κB and MAPK signaling by targeting Map3k7, which attenuates LPS-induced ALI (Yang et al. 2022). In mouse macrophages, knockdown of Map3k7 inhibits the expression of IL-33 and IL-1, which alleviate lung inflammation induced by black carbon (Cheng et al. 2019). Li and colleagues have confirmed that inhibition of Map3k7 significantly reduces the expression of inflammatory cytokines (IL-1β, TNF-α, and TGF-β) in alveolar macrophage NR8383 cells after exposure to silica, which could alleviate inflammation and pulmonary fibrosis in pneumoconiosis (Li et al. 2017). The novel Map3k7 inhibitor handelin inhibits pro-inflammatory mediators mediated by NF-κB and AP-1 to alleviate the development of elastase-induced emphysema in mice (Yun et al. 2023).

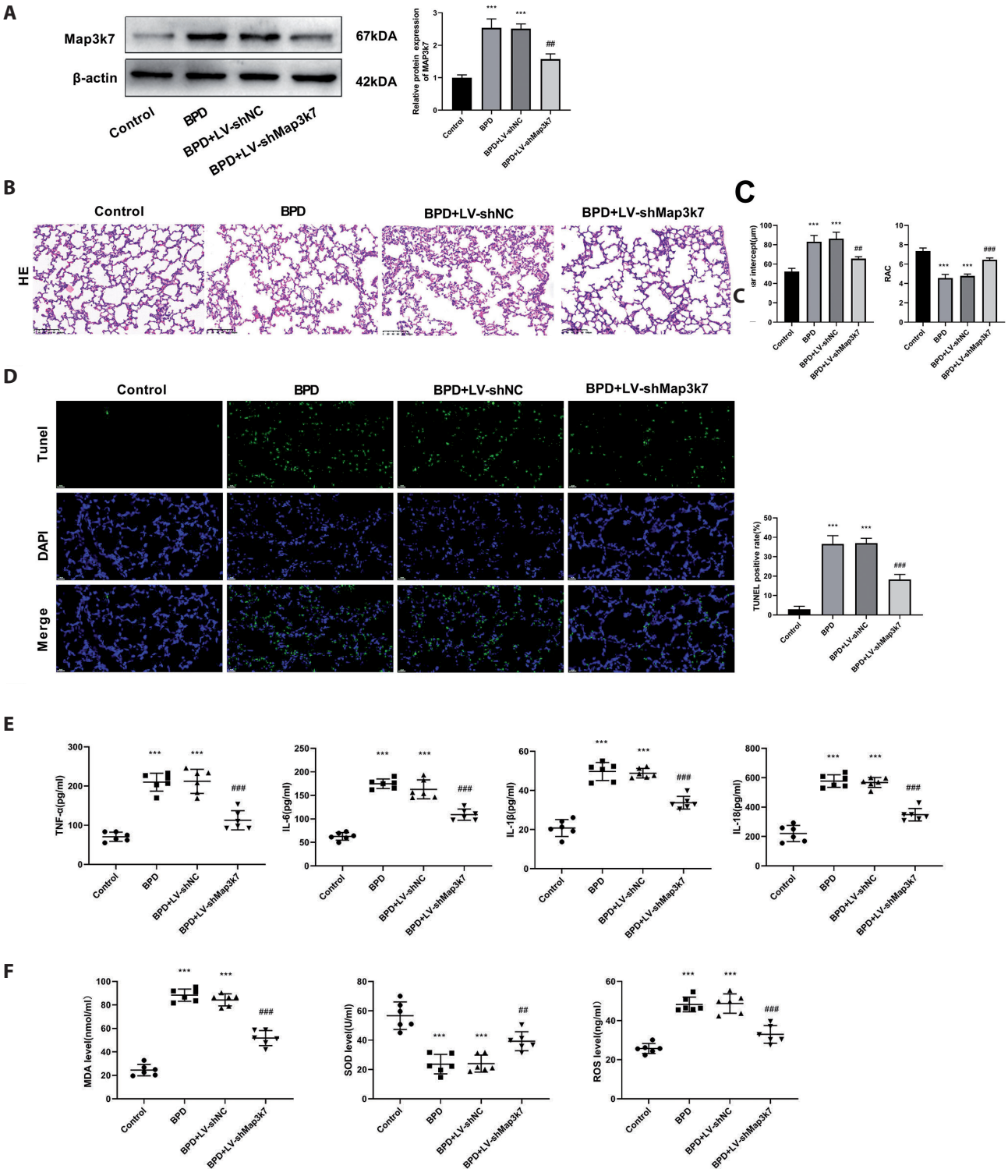

Figure 7. Silencing Map3k7 alleviated BPD progression *in vivo*. **A.** Western blot was employed to quantify the expression levels of Map3k7 protein. **B.** Hematoxylin and Eosin (HE) staining was utilized to visualize rat lung tissue (Scale: 100 μm, magnification: 200×). **C.** The Mean Linear Intercept (MLI) and Radial Alveolar Count (RAC) were measured. **D.** TUNEL fluorescent staining was performed to evaluate the levels of apoptotic cells in rat lung tissue (scale: 20 μm, magnification: 400×). **E.** ELISA was conducted to determine the expression levels of inflammatory factors (TNF-α, IL-6, IL-18 and IL-1β). **F.** ELISA was also used to quantify the levels of oxidative stress indicators (MDA, SOD and ROS). *** $p < 0.001$ *vs.* Control; $^{###}$ $p < 0.001$, $^{##}$ $p < 0.01$ *vs.* BPD+LV-shNC ($n = 6$).

In concurrence to the abovementioned results, in this study, silencing Map3k7 significantly decreased the levels of inflammatory cytokines (TNF-α, IL-1β, IL-18, and IL-6) and oxidative stress indicators compared with those in the hyperoxia group. This indicates that silencing Map3k7 can alleviate inflammation and oxidative stress in BPD.

Pyroptosis is programmed cell death dependent on cysteine aspartic proteases (caspase-1/4/5/11) (Bergsbaken et al. 2009; Shi et al. 2017). Pyroptosis mainly mediates the activation of various caspases through inflammasomes, which cause cleavage and polymerization of members of the gasdermin family, including GSDMD, resulting in cell perforation and death (Kovacs et al. 2017). NLRP3 is a more abundant and typical inflammasome in current studies on pyroptosis. Blocking macrophage pyroptosis by inhibiting NLRP3 or caspase-1 reduces silica-mediated lung inflammation and fibrosis (Peukert et al. 2022, Yin et al. 2022). Currently, evidence of pyroptosis correlating with the pathogenesis of various respiratory diseases has increased. Map3k7 regulates NLRP3-mediated neuronal pyroptosis in early brain injury, and inhibition of Map3k7 can alleviate the neuroinflammatory response induced by subarachnoid hemorrhage (Xu et al. 2021). Similar to the abovementioned results, silencing Map3k7 reduced the expression of pyroptosis-related proteins in hyperoxia-induced BPD cells, illustrating that silencing Map3k7 may affect BPD by inhibiting pyroptosis. Moreover, TGF-β1 participates in the regulation of pyroptosis in diseases. Silencing the long-chain noncoding RNA Kcnq1ot1 inhibits TGF-β1/Smad3 pathway and pyroptosis, thereby ameliorating myocardial fibrosis in diabetic mice (Yang et al. 2018). Xie et al. (2022) have reported that TGF-β1 attenuates pyroptosis of microglia by NF-κB/ERK1/2 pathway to alleviate LPC-induced demyelination and cognitive deficits. MiR-342-3p inhibits HK-2 cell pyroptosis by suppressing the TGF-β/SMAD axis, thereby mitigating renal injury (Yang et al. 2023). Herein, silencing Map3k7 significantly decreased the TGF-β1/Smad3 pathway related proteins, and SRI-011381 (the TGF-β1 pathway activator) weakened the inhibitory effects of silencing Map3k7 on pyroptosis in hyperoxia-induced AEC-II, indicating that Map3k7 may regulate pyroptosis through TGF-β1/Smad3 pathway, thus affecting the progression of BPD.

In conclusion, through in vivo and in vitro assays, silencing Map3k7 promoted cell proliferation and reduced inflammation, oxidative stress, and pyroptosis in hyperoxia-induced BPD. Additionally, feedback experiments demonstrated that silencing MAP3K7 may suppress pyroptosis to alleviate BPD progression through inhibition of the TGF-β1/Smad3 pathway. Map3k7 may be a key factor in the pathogenesis of BPD, providing a direction for the prevention and treatment of BPD in premature infants.

Funding. Guangxi Natural Science Foundation Project (No. 2022GXNSFAA035514).

Conflicts of interest. The authors declare that they have no conflicts of interest to disclose.

Ethical approval and consent to participate. The animal experiments conformed to the Guide for the Care and Use of Laboratory Animals. Animal study has been approved by the Animal Ethics Committee of the second affiliated hospital of Guangxi medical university (2022, KY-0095). All experiments were performed in accordance with relevant guidelines and regulations. The manuscript reporting adheres to the ARRIVE guidelines for the reporting of animal experiments.

Availability statement. The datasets generated and/or analyzed during the current study are available in the [NCBI] repository, [http://www.ncbi.nlm.nih.gov/bioproject/1136235].

Authors' contributions. HZ: substantial contributions to conception and design, data acquisition, drafting the article; QW and BW: data acquisition, drafting the article; QH and RL: data acquisition; reviewing the article. All the authors took part in the experiment and read and approved the manuscript.

References

Ajibade AA, Wang HY, Wang RF (2013): Cell type-specific function of TAK1 in innate immune signaling. Trends Immunol. **340,** 307-316 https://doi.org/10.1016/j.it.2013.03.007

Baker CD, Alvira CM (2014): Disrupted lung development and bronchopulmonary dysplasia: opportunities for lung repair and regeneration. Curr. Opin. Pediatr. **26,** 306-314 https://doi.org/10.1097/MOP.0000000000000095

Bergsbaken T, Fink SL, Cookson BT (2009): Pyroptosis: host cell death and inflammation. Nat. Rev. Microbiol. **7,** 99-109 https://doi.org/10.1038/nrmicro2070

Bhandari A, Panitch HB (2006): Pulmonary outcomes in bronchopulmonary dysplasia. Semin. Perinatol. **30,** 219-226 https://doi.org/10.1053/j.semperi.2006.05.009

Chakraborty M, McGreal EP, Williams A, Davies PL, Powell W, Abdulla S, Voitenok NN, Hogwood J, Gray E, Spiller B, et al. (2014): Role of serine proteases in the regulation of interleukin-877 during the development of bronchopulmonary dysplasia in preterm ventilated infants. PLoS One **9,** e114524 https://doi.org/10.1371/journal.pone.0114524

Chen X, Zhao Y, Wang X, Lin Y, Zhao W, Wu D, Pan J, Luo W, Wang Y, Liang G (2022): FAK mediates LPS-induced inflammatory lung injury through interacting TAK1 and activating TAK1-NFkappaB pathway. Cell Death Dis. **13,** 589 https://doi.org/10.1038/s41419-022-05046-7

Cheng Y, Li S, Wang M, Cheng C, Liu R (2018): Peroxisome proliferator activated receptor gamma (PPARγ) agonist Rosiglitazone ameliorate airway inflammation by inhibiting toll-like receptor 2 (TLR2)/Nod-like receptor with pyrin domain containing 3 (NLRP3) inflammatory corpuscle activation in asthmatic mice. Med. Sci. Monit. **24,** 9045-9053

https://doi.org/10.12659/MSM.910766
Cheng Z, Chu H, Wang S, Huang Y, Hou X, Zhang Q, Zhou W, Jia L, Meng Q, Shang L, et al. (2019): TAK1 knock-down in macrophage alleviate lung inflammation induced by black carbon and aged black carbon. Environ. Pollut. **253,** 507-515 https://doi.org/10.1016/j.envpol.2019.06.096
Crisford H, Sapey E, Stockley RA (2018): Proteinase 3; a potential target in chronic obstructive pulmonary disease and other chronic inflammatory diseases. Respir. Res. **19,** 180 https://doi.org/10.1186/s12931-018-0883-z
Eltom S, Belvisi MG, Stevenson CS, Maher SA, Dubuis E, Fitzgerald KA, Birrell MA (2014): Role of the inflammasome-caspase1/11-IL-1/18 axis in cigarette smoke driven airway inflammation: an insight into the pathogenesis of COPD. PLoS One **9,** e112829 https://doi.org/10.1371/journal.pone.0112829
Guo H, Callaway JB, Ting JP (2015): Inflammasomes: mechanism of action, role in disease, and therapeutics. Nat. Med. **21,** 677-687 https://doi.org/10.1038/nm.3893
Hurskainen M, Mižíková I, Cook DP, Andersson N, Cyr-Depauw C, Lesage F, Helle E, Renesme L, Jankov RP, Heikinheimo M, et al. (2021): Single cell transcriptomic analysis of murine lung development on hyperoxia-induced damage. Nat. Commun. **12,** 1565 https://doi.org/10.1038/s41467-021-21865-2
Hussain S, Sangtian S, Anderson SM, Snyder RJ, Marshburn JD, Rice AB, Bonner JC, Garantziotis S (2014): Inflammasome activation in airway epithelial cells after multi-walled carbon nanotube exposure mediates a profibrotic response in lung fibroblasts. Part Fibre Toxicol. **11,** 28 https://doi.org/10.1186/1743-8977-11-28
Jensen EA, Schmidt B (2014): Epidemiology of bronchopulmonary dysplasia. Birth Defects Res. A Clin. Mol. Teratol. **100,** 145-157 https://doi.org/10.1002/bdra.23235
Kalymbetova TV, Selvakumar B, Rodríguez-Castillo JA, Gunjak M, Malainou C, Heindl MR, Moiseenko A, Chao CM, Vadász I, Mayer K, et al. (2018): Resident alveolar macrophages are master regulators of arrested alveolarization in experimental bronchopulmonary dysplasia. J. Pathol. **245,** 153-159 https://doi.org/10.1002/path.5076
Kovacs SB, Miao EA (2017): Gasdermins: Effectors of pyroptosis. Trends Cell Biol. **27,** 673-684 https://doi.org/10.1016/j.tcb.2017.05.005
Kwon JH, Kim M, Bae YK, Kim GH, Choi SJ, Oh W, Um S, Jin HJ (2019): Decorin secreted by human umbilical cord blood-derived mesenchymal stem cells induces macrophage polarization via CD44 to repair hyperoxic lung injury. Int. J. Mol. Sci. **20,** 4815 https://doi.org/10.3390/ijms20194815
Kwong KY, Niang S, Literat A, Zhu NL, Ramanathan R, Jones CA, Minoo P (2006): Expression of transforming growth factor beta (TGF-b1) by human preterm lung inflammatory cells. Life Sci. **79,** 2349-2356 https://doi.org/10.1016/j.lfs.2006.07.040
Lamkanfi M, Dixit VM (2014): Mechanisms and functions of inflammasomes. Cell **157,** 1013-1022 https://doi.org/10.1016/j.cell.2014.04.007
Li D, Ren W, Jiang Z, Zhu L (2018): Regulation of the NLRP3 inflammasome and macrophage pyroptosis by the p38 MAPK signaling pathway in a mouse model of acute lung injury. Mol. Med. Rep. **18,** 4399-4409 https://doi.org/10.3892/mmr.2018.9427
Li J, Liang C, Zhang ZK, Pan X, Peng S, Lee WS, Lu A, Lin Z, Zhang G, Leung WN, Zhang BT (2017): TAK1 inhibition attenuates both inflammation and fibrosis in experimental pneumoconiosis. Cell Discov. **3,** 17023 https://doi.org/10.1038/celldisc.2017.23
Liu X, Huang X, Xu F (2023): The influence of pyroptosis-related genes on the development of chronic obstructive pulmonary disease. BMC Pulm. Med. **23,** 167 https://doi.org/10.1186/s12890-023-02408-5
Mihaly SR, Ninomiya-Tsuji J, Morioka S (2014): TAK1 control of cell death. Cell Death Differ. **21,** 1667-1676 https://doi.org/10.1038/cdd.2014.123
Mukhopadhyay H, Lee NY (2020): Multifaceted roles of TAK1 signaling in cancer. Oncogene **39,** 1402-1413 https://doi.org/10.1038/s41388-019-1088-8
Pera T, Atmaj C, van der Vegt M, Halayko AJ, Zaagsma J, Meurs H (2012): Role for TAK1 in cigarette smoke-induced proinflammatory signaling and IL-8 release by human airway smooth muscle cells. Am. J. Physiol. Lung Cell. Mol. Physiol. **303,** L272-278 https://doi.org/10.1152/ajplung.00291.2011
Peukert K, Steinhagen F, Fox M, Feuerborn C, Schulz S, Seeliger B, Schuss P, Schneider M, Frede S, Sauer A, et al. (2022): Tetracycline ameliorates silica-induced pulmonary inflammation and fibrosis via inhibition of caspase-1. Respir. Res. **23,** 21 https://doi.org/10.1186/s12931-022-01937-7
Shi J, Gao W, Shao F (2017): Pyroptosis: Gasdermin-mediated programmed necrotic cell death. Trends Biochem. Sci. **42,** 245-254 https://doi.org/10.1016/j.tibs.2016.10.004
Shi L, Xin Q, Chai R, Liu L, Ma Z (2015): Ectopic expressed miR-203 contributes to chronic obstructive pulmonary disease via targeting TAK1 and PIK3CA. Int. J. Clin. Exp. Pathol. **8,** 10662-10670
Shukla VV, Ambalavanan N (2021): Recent advances in bronchopulmonary dysplasia. Indian J. Pediatr. **88,** 690-695 https://doi.org/10.1007/s12098-021-03766-w
Song M, Wang J, Sun Y, Pang J, Li X, Liu Y, Zhou Y, Yang P, Fan T, Liu Y, et al. (2022): Inhibition of gasdermin D-dependent pyroptosis attenuates the progression of silica-induced pulmonary inflammation and fibrosis. Acta Pharm. Sin. B **12,** 1213-1224 https://doi.org/10.1016/j.apsb.2021.10.006
Takaesu G, Surabhi RM, Park KJ, Ninomiya-Tsuji J, Matsumoto K, Gaynor RB (2003): TAK1 is critical for IkappaB kinase-mediated activation of the NF-kappaB pathway. J. Mol. Biol. **326,** 105-115 https://doi.org/10.1016/S0022-2836(02)01404-3
Wang Y, Jin Z, Jia S, Shen P, Yang Y, Huang Y (2023): Mechanical stress protects against chondrocyte pyroptosis through TGF-β1-mediated activation of Smad2/3 and inhibition of the NF-κB signaling pathway in an osteoarthritis model. Biomed. Pharmacother. **159,** 114216 https://doi.org/10.1016/j.biopha.2023.114216

Wu DD, Pan PH, Liu B, Su XL, Zhang LM, Tan HY, Cao Z, Zhou ZR, Li HT, Li HS, et al. (2015): Inhibition of alveolar macrophage pyroptosis reduces lipopolysaccharide-induced acute lung injury in mice. Chin. Med. J. (Engl) **128,** 2638-2645 https://doi.org/10.4103/0366-6999.166039

Xie Y, Chen X, Li Y, Chen S, Liu S, Yu Z, Wang W (2022): Transforming growth factor-β1 protects against LPC-induced cognitive deficit by attenuating pyroptosis of microglia via NF-κB/ERK1/2 pathways. J. Neuroinflam. **19,** 194 https://doi.org/10.1186/s12974-022-02557-0

Xu P, Tao C, Zhu Y, Wang G, Kong L, Li W, Li R, Li J, Zhang C, Wang L, et al. (2021): TAK1 mediates neuronal pyroptosis in early brain injury after subarachnoid hemorrhage. J. Neuroinflam. **18,** 188 https://doi.org/10.1186/s12974-021-02226-8

Xu YR, Lei CQ (2020): TAK1-TABs Complex: a central signalosome in inflammatory responses. Front. Immunol. **11,** 608976 https://doi.org/10.3389/fimmu.2020.608976

Yamaguchi K, Shirakabe K, Shibuya H, Irie K, Oishi I, Ueno N, Taniguchi T, Nishida E, Matsumoto K (1995): Identification of a member of the MAPKKK family as a potential mediator of TGF-beta signal transduction. Science **270,** 2008-2011 https://doi.org/10.1126/science.270.5244.2008

Yang F, Qin Y, Lv J, Wang Y, Che H, Chen X, Jiang Y, Li A, Sun X, Yue E, et al. (2018): Silencing long non-coding RNA Kcnq1ot1 alleviates pyroptosis and fibrosis in diabetic cardiomyopathy. Cell Death Dis. **90,** 1000 https://doi.org/10.1038/s41419-018-1029-4

Yang J, Li B, Wang J, Fan W (2023): Puerarin alleviates chronic renal failure-induced pyroptosis in renal tubular epithelial cells by targeting miR-342-3p/TGF-β/SMAD axis. Genes Genomics **45,** 1563-1573 https://doi.org/10.1007/s13258-023-01448-9

Yang YC, Zhang MY, Liu JY, Jiang YY, Ji XL, Qu YQ (2022): Identification of ferroptosis-related Hub genes and their association with immune infiltration in chronic obstructive pulmonary disease by bioinformatics analysis. Int. J. Chron. Obstruct. Pulmon. Dis. **17,** 1219-1236 https://doi.org/10.2147/COPD.S348569

Yin H, Fang L, Wang L, Xia Y, Tian J, Ma L, Zhang J, Li N, Li W, Yao S, Zhang L (2022): Acute silica exposure triggers pulmonary inflammation through macrophage pyroptosis: An experimental simulation. Front. Immunol. **13,** 874459 https://doi.org/10.3389/fimmu.2022.874459

Yun HJ, Lee HY (2023): The novel TAK1 inhibitor handelin inhibits NF-κB and AP-1 activity to alleviate elastase-induced emphysema in mice. Life Sci. **319,** 121388 https://doi.org/10.1016/j.lfs.2023.121388

Zhang Z, Chen K, Pan D, Liu T, Hang C, Ying Y, He J, Lv Y, Ma X, Chen Z, et al. (2023): A predictive model for preterm infants with bronchopulmonary dysplasia based on ferroptosis-related lncRNAs. BMC Pulm. Med. **23,** 367 https://doi.org/10.1186/s12890-023-02670-7

Received: July 19, 2024
Final version accepted: October 21, 2024

doi: 10.4149/gpb_2024043

Supplementary Material

Silencing Map3k7 suppresses pyroptosis to alleviate bronchopulmonary dysplasia through inhibiting the TGF-β1/Smad3 pathway

Hong Zhen[1], Qiaozhen Wei[1], Bingmei Wei[1], Qingmei Huang[1] and Ruishan Li[1]

[1] *Department of Pediatrics, The Second Affiliated Hospital of Guangxi Medical University, Nanning, Guangxi Province, China*

Supplementary Figures

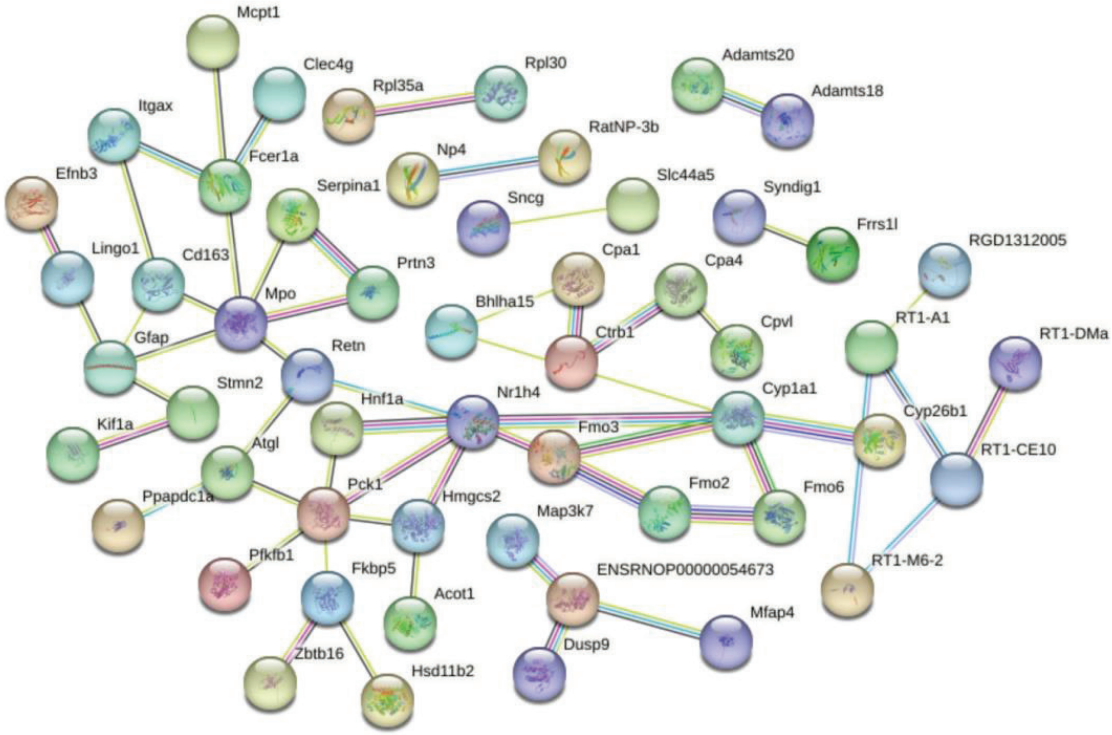

Figure S1. Protein-protein interaction network analysis. Lines between nodes represent interactions between genes.

Table S1. Primer sequences

Name	Sequence (5'–3')
Gapdh-F	GAGTCAACGGATTTGGTCGT
Gapdh-R	TTGATTTTGGAGGGATCTCG
Map3k7-F	ACAGTGTTCCCAAGGAGTGG
Map3k7-R	AACTTCAGGTGCCATCCAAG
Itgax -F	AGAATTGTCCATGGCTCCAC
Itgax -R	GGTGGTGCATAATGTTGCTG
Prtn3 -F	GCGACTAGCAACCAAGGAAC
Prtn3-R	CATTTTGGGCTTGTTCCAGT
Cd163-F	CTCCAGCATTACACCCACCT
Cd163-R	GGAGATTTTGAGCCCTTTCC
Nlrp3-F:	ATCAACAGGCGAGACCTCTG
Nlrp3-R	GTCCTCCT GGCATACCATAGA
Asc-F	GACAGTACCAGGCAGTTCGT
Asc-R	AGTAGGGCTGTGTTT GCCTC
Caspase-1-F	GCTTTCTGCTCTTCCACACC
Caspase-1-R	CATCTGGCTGCTCAAATGAA
Gsdmd-F	GGTTCTGGAAACCCCGTTAT
Gsdmd-R	CCAGGTGTTAGGGTCCACAC

Table S2. Top 10 up and down-regulated DEGs

Name	Description	log2FC	*p* value	up/down
Plpp4	phospholipid phosphatase 4	4.313177192	1.04161E−14	up
Rhox5	Rhox homeobox family member 5	4.0631906	0.036456877	up
Hnf1a	HNF1 homeobox A	4.062553555	0.047938151	up
Cntn6	contactin 6	3.854413809	0.047299716	up
Cdh16	cadherin 16	3.622421629	0.012728146	up
Robo3	roundabout guidance receptor 3	3.58835831	0.035429053	up
Adamts20	ADAM metallopeptidase with thrombospondin type 1 motif, 20	3.489064344	0.004199863	up
Snx31	sorting nexin 31	3.220993686	0.023816299	up
RT1-M6-2	RT1 class I, locus M6, gene 2	2.968121138	1.05779E−08	up
Trim67	tripartite motif-containing 67	2.967634972	0.020576648	up
Lpo	lactoperoxidase	−5.066675595	3.67344E−07	down
Gal	galanin and GMAP prepropeptide	−4.061819536	0.000445787	down
RT1-DMa	RT1 class II, locus DMa	−4.002038738	0.049744242	down
LOC100911615	patatin-like phospholipase domain-containing protein 2-like	−3.603675714	0.000153931	down
Gpr15	G protein-coupled receptor 15	−3.493963497	0.003213659	down
Akap3	A-kinase anchoring protein 3	−3.466203749	0.021810161	down
Vom2r44	vomeronasal 2 receptor 44	−2.945655718	0.032053167	down
Mlc1	modulator of VRAC current 1	−2.855378103	7.22476E−14	down
Fmo6	flavin containing monooxygenase 6	−2.58852489	0.022509843	down
Hif3α	hypoxia inducible factor 3 subunit alpha	−2.532304133	9.6698E−20	down

Table S3. GO enrichment analysis of DEGs

GO term	Subgroup	–log10(*p* value)
GO:0015893 drug transport	Biological process	5.429855988
GO:0009620 response to fungus	Biological process	5.124452705
GO:0050832 defense response to fungus	Biological process	5.110309368
GO:0002476 antigen processing and presentation of endogenous	Biological process	5.025189505
GO:0002428 antigen processing and presentation of peptide antigen	Biological process	4.943579695
GO:0002475 antigen processing and presentation via MHC class Ib	Biological process	4.717279478
GO:0005615 extracellular space	Cellular component	10.06238563
GO:0005576 extracellular region	Cellular component	9.65195566
GO:0097449 astrocyte projection	Cellular component	5.387708299
GO:0097450 astrocyte end-foot	Cellular component	4.913877307
GO:0016323 basolateral plasma membrane	Cellular component	4.473904297
GO:0097386 glial cell projection	Cellular component	4.347255645
GO:0016661 oxidoreductase activity	Molecular function	4.452939595
GO:0004499 N,N-dimethylaniline monooxygenase activity	Molecular function	4.079260516
GO:0016709 oxidoreductase activity, acting on paired donors	Molecular function	4.04183143
GO:0016662 oxidoreductase activity, acting on other nitrogenous	Molecular function	3.21453409
GO:0050421 nitrite reductase (NO-forming) activity	Molecular function	3.21453409
GO:0098809 nitrite reductase activity	Molecular function	3.21453409

Table S4. KEGG enrichment analysis of DEGs

KEGG term	rich	FDR	Number
Staphylococcus aureus infection	0.058823529	4.55E–02	5
Bile secretion	0.063291139	3.67E–02	5
Phagosome	0.046052632	0.03541393	7
Antigen processing and presentation	0.085714286	0.003254343	6
Viral myocarditis	0.089552239	0.002971263	6
Cell adhesion molecules	0.060402685	0.001601836	9
Autoimmune thyroid disease	0.115384615	0.001044964	6
Type I diabetes mellitus	0.117647059	0.001044964	6
Allograft rejection	0.133333333	0.000892309	6
Graft-*versus*-host disease	0.136363636	0.000892309	6